Transformation processes in $LaAlO_3$: Neutron diffraction, dielectric, thermal, optical, and Raman studies

S. A. Hayward,[1] F. D. Morrison,[1] S. A. T. Redfern,[1] E. K. H. Salje,[1] J. F. Scott,[1] K. S. Knight,[2] S. Tarantino,[3] A. M. Glazer,[4] V. Shuvaeva,[4] P. Daniel,[5] M. Zhang,[1] and M. A. Carpenter[1]

[1]*Department of Earth Sciences, University of Cambridge, Downing Street, Cambridge CB2 3EQ, United Kingdom*

[2]*ISIS Neutron Facility, Rutherford Appleton Laboratory, Chilton, Didcot OX11 0QX, United Kingdom*

[3]*Dipartimento di Scienze della Terra, Università di Pavia, Via Ferrata 1, 27100 Pavia, Italy*

[4]*Department of Physics, University of Oxford, Clarendon Laboratory, Parks Road, Oxford, OX1 3PU, United Kingdom*

[5]*Laboratoire de Physique de l'Etat Condensé, Université du Maine, 72085 Le Mans Cedex 9, France*

(Received 7 January 2005; revised manuscript received 10 June 2005; published 4 August 2005)

The behavior of the $Pm\bar{3}m$-$R\bar{3}c$ phase transition in $LaAlO_3$ (T_C=813 K from differential scanning calorimetry measurements) has been studied using temperature-dependent measurements of the crystal structure, dielectric relaxation, specific heat, birefringence, and the frequencies of the two soft modes (via Raman spectroscopy). While all these experiments show behavior near T_C consistent with a second-order Landau transition, there is extensive evidence for additional anomalous behavior below 730 K. Below this temperature, the two soft mode frequencies are not proportional to each other, the spontaneous strain is not proportional to the square of the AlO_6 rotation angle, and anomalies are seen in the birefringence. Twin domains, which are mobile above 730 K, are frozen below 730 K. These anomalies are consistent with biquadratic coupling between the primary order parameter of the transition (AlO_6 rotation) and a second process. From the dielectric results, which indicate a smooth but rapid increase in conductivity in the temperature range 500–800 K, we propose that this second process is hopping of intrinsic oxygen vacancies. These vacancies are essentially static below 730 K and dynamically disordered above 730 K. The interaction between static vacancies and the displacive phase transition is unfavorable. A similar anomaly may be observed in other aluminate perovskites undergoing the same transition.

DOI: 10.1103/PhysRevB.72.054110 PACS number(s): 61.50.Ks, 64.70.Kb

I. INTRODUCTION

The role of strain in structural phase transitions remains fundamental to understanding the properties of framework structures such as perovskites. In general, spontaneous strains act either as the primary driving order parameter themselves (true proper ferroelastics), or they arise from coupling with a different driving order parameter which they "slave" (pseudoproper ferroelastics, improper ferroelastics, and coelastics). A general consequence of strain coupling is that the order parameter extends over a characteristic correlation length which is determined by the long-ranging strain fields. As a result, mean field behavior dominates, and so phase transitions with significant spontaneous strains usually follow models derived from the Landau theory very closely.[1–3] A second consequence of the coupling between the order parameter and strain is that the strain provides a mechanism for coupling between the order parameters of two or more phase transition processes. The temperature evolution of the order parameters is modified by the coupling; the exact nature of this modification depends on the strength and symmetry of the coupling term. In ferroelastic and coelastic crystals, the spontaneous strains are related to the order parameter, with a mathematical form defined by the form of the strain-order parameter coupling energy.[4] In the vast majority of cases, the relationship is rather simple; either the strain e is proportional to the order parameter Q, or $e \propto Q^2$. In these cases, the spontaneous strain is effectively another manifestation of the order parameter.

The cubic-rhombohedral phase transition in $LaAlO_3$ is an improper ferroelastic. The main structural difference between the cubic and rhombohedral phases is the rotation of AlO_6 octahedra around one of the triad axes in the cubic phase, as shown in Fig. 1. In the notation of Glazer,[5] this tilt system is $a^-a^-a^-$. Breaking the cubic symmetry allows these octahedra to become distorted, becoming elongated or squashed along the rotation axis. Unless the elastic and coupling constants have very specific values, Darlington[6] shows that octahedral distortion is energetically favorable, and that the distortion of the octahedra [$(1-\eta)$, as described in Sec. II D below] should be proportional to ϕ^2.

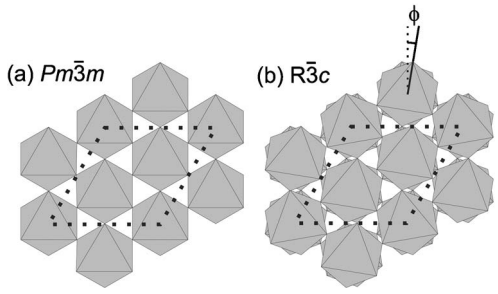

FIG. 1. Schematic representation of the AlO_6 polyhedral network in (a) cubic and (b) rhombohedral $LaAlO_3$, viewed down $[001]_{trigonal}$, equivalent to $\langle 111 \rangle_{cubic}$. All polyhedra rotate through the same angle ϕ, with half the polyhedra rotating clockwise around the triad axis, and half rotating anticlockwise.

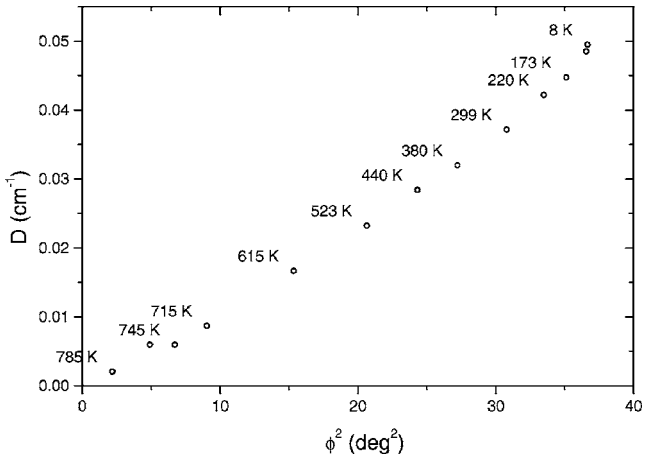

FIG. 2. EPR spectroscopic data for the phase transition in $LaAlO_3$, with the EPR splitting D (which measures the distortion of the AlO_6 units) plotted against the square of the AlO_6 rotation angle. Data from Ref. 9.

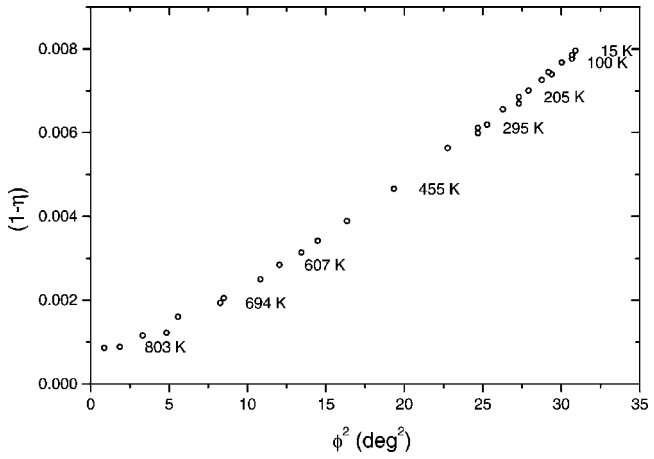

FIG. 3. Neutron diffraction data for the phase transition in $LaAlO_3$, with the distortion of the AlO_6 units plotted against the square of the AlO_6 rotation angle. Data from Ref. 10.

A wide range of experimental data exist for the phase transition in $LaAlO_3$, first identified by optical microscopy and x-ray powder diffraction.[7,8] These data include measurements of the AlO_6 rotation angle by electron paramagnetic resonance (EPR) spectroscopy,[9] neutron diffraction,[10–12] and x-ray diffraction.[12,13] The spontaneous strain has been measured using x-ray rocking curves.[14,15] The temperature dependence of the soft modes has been determined using Raman spectroscopy.[16] The phase transition is also induced by high pressures at ambient temperature,[17,18] but the experimental data on the effect of pressure are much less extensive.

The various experiments show a good agreement where they measure the same property; for example, the measurements of the AlO_6 rotation angle by EPR[9] show similar behavior to diffraction measurements of the same quantity.[10,11] The differences that are observed are of the order of 10%, and are almost certainly due to calibration effects. However, the expected proportionalities between different aspects of the phase transition are not observed. For example, the EPR study of Müller *et al.*[9] measured both the AlO_6 rotation angle and the EPR axial splitting D, which reflects the local distortion of octahedra along the triad axis. Simple coupling theory predicts $D \propto \phi^2$. As shown in Fig. 2, this proportionality is not observed, if the entire data set is considered. This discrepancy was interpreted[9] by invoking critical fluctuations to modify the temperature dependence of $\phi(T)$. Howard *et al.*[10] obtained a similar result from their neutron diffraction experiments (Fig. 3). In short, while $(1-\eta) \propto \phi^2$ is seen at some temperatures (generally those close to T_C), it does not apply over the whole temperature range.

Hayward *et al.*[15] investigated the same issue from a different perspective. At low temperatures, the order parameter is expected to saturate, as the phase transition reaches its zero-point ground state. For the simplest second-order phase transition with quantum saturation, the temperature dependence of the order parameter for flat phonon dispersion is given by[19,20]

$$Q^2 = 1 - \frac{1}{T_C}\left[\theta_S \coth\left(\frac{\theta_S}{T}\right)\right] \approx 1 - \frac{T}{T_C} \text{ for } T \gg \theta_S. \quad (1)$$

Fitting the various available data to this model gave different values of θ_S, varying from 95 K to 260 K. Hayward *et al.*[15] argued that these data could be explained by considering the rotation and distortion of the octahedra separately and allowing these two processes to have different temperature dependencies. While some experimental measurements depend on only one or another process, others (such as the total spontaneous strain) depend on some combination of the two.

It is clear that the phase transition in $LaAlO_3$ does not follow "simple" Landau-like second-order behavior (that is, controlled by a single order parameter) over the entire temperature range. However, there are several possible forms for this anomalous behavior, and it is not immediately clear which model is an appropriate description of the discrepancy. It could be that the exponent in the coupling relationship $(1-\eta) \propto \phi^n$ is not strictly 2, or that the classical model is applicable at high temperatures but deviates at low T due to quantum mechanical effects, or that a complex order parameter topology[21] applies. The existing data are mostly too sparse to distinguish between these possibilities, either because they cover a limited temperature range, or because data points are too widely spaced in T.

In a number of systematic surveys of ferroelastic and coelastic phase transitions, it has been shown that anomalies in a wide range of experimental measurements have essentially the same behavior. Examples include leucite,[22] $SrTiO_3$ (Refs. 23 and 24) and lawsonite.[25] In this study, we apply a similar approach to $LaAlO_3$, in order to identify the precise nature and origin of the anomalies outlined above. We report new high-resolution neutron diffraction data, collected at 10 K intervals between 4.2 K and 1270 K. We compare these data with the results of dielectric, calorimetric, birefringence, and Raman measurements. We show that the critical behavior of $LaAlO_3$ (from 100 K below the transition temperature up to T_C) is fully consistent with a Landau model, but that deviations occur at lower temperatures. We describe the quantitative form of this anomaly and investigate a possible physical mechanism. We then apply these insights to the available experimental data for other systems.

II. NEUTRON DIFFRACTION

A. Experimental details

The samples used in this study were from a batch grown by the Czochralski method by Crystal Gmbh (Berlin). For the neutron diffraction experiments, several large pieces of pink $LaAlO_3$ crystal were selected. These crystals were hand-ground, sieved, and washed to give a powder with grain sizes in the range 10–40 μm. The color of $LaAlO_3$ crystals varies between colorless and brown, depending on the thermal history of the sample; the color of $LaAlO_3$ crystals is associated with oxygen vacancies.[26] Initially colorless samples of $LaAlO_3$ are found to turn brown when heated in air at around 440 °C for approximately 5 min.[27]

Powder neutron diffraction patterns were collected at temperatures between 4.2 K and 1270 K on the high-resolution powder diffractometer (HRPD) at the ISIS spallation source.[28] Approximately 1 cm^3 of $LaAlO_3$ powder was enclosed in a thin-walled vanadium sample can with 11 mm internal diameter. This can was first connected to a standard ISIS cryofurnace, which operates in the temperature range 4.2–620 K. Spectra were collected with the sample in the cryofurnace between 4.2 K and 620 K. A standard ISIS furnace was used to collect data in the temperature range from room temperature to 1270 K.

Time-of-flight data were collected in two detector banks of ZnS scintillators. The backscattering bank centered on $2\theta=168°$ gives a resolution $\Delta d/d=4-5\times10^{-4}$ in a d-spacing range 0.6–4.6 Å. The 90° bank has a resolution $\Delta d/d=2\times10^{-3}$ and a useful d-spacing range 0.9–6.6 Å. Data at each temperature step were collected until a fixed integrated intensity had been collected, which corresponded to approximately 15 min of count time with a full beam.

Spectra were collected with the sample in the cryofurnace at 4.2 K, 10 K, and then in 10 K steps to 620 K. The sample furnace was then used to record the diffraction pattern at room temperature and at 10 K steps between 700 K and 1270 K. In order to provide a check on the comparability of the data from the two sample holders, a final spectrum was collected running the sample furnace at 600 K. No significant differences were found between the structures refined from data collected using the two different sample holders.

All the diffraction patterns were analyzed using the Rietveld method by the GSAS software package.[29] The refinement parameters were the background coefficients and intensity scaling, then the lattice parameters, peak shapes, free atomic co-ordinate (where appropriate), and thermal parameters (isotropic for La and Al, anisotropic for O). For the high-temperature structure, the perovskite aristotype structure was fixed in the refinement, with the lattice parameter a as the only free structural parameter. Some spectra recorded just below the transition temperature were also refined on the cubic cell; however, these refinements were not satisfactory, since fitting split pairs of peaks to a single peak led to unrealistic peak profile parameters. The low-temperature structure was taken to be the $R\bar{3}c$ perovskite structure, refined on the trigonal co-ordinate set. In this structure, there are two free lattice parameters (a_T and c_T), and one free atomic co-ordinate (the x co-ordinate of the O site). For the spontaneous strain analysis which follows, these structures were subsequently converted to the pseudocubic F-centered rhombohedral unit cell ($a_{PC}=b_{PC}=c_{PC}, \alpha_{PC}=\beta_{PC}=\gamma_{PC}\neq90°$). The relationships between the lattice parameters of the two cells are

$$a_{PC}=\frac{(c_T^2+12a_T^2)^{1/2}}{3}, \tag{2}$$

$$\cos\alpha_{PC}=\frac{(c_T^2-6a_T^2)}{c_T^2+12a_T^2}. \tag{3}$$

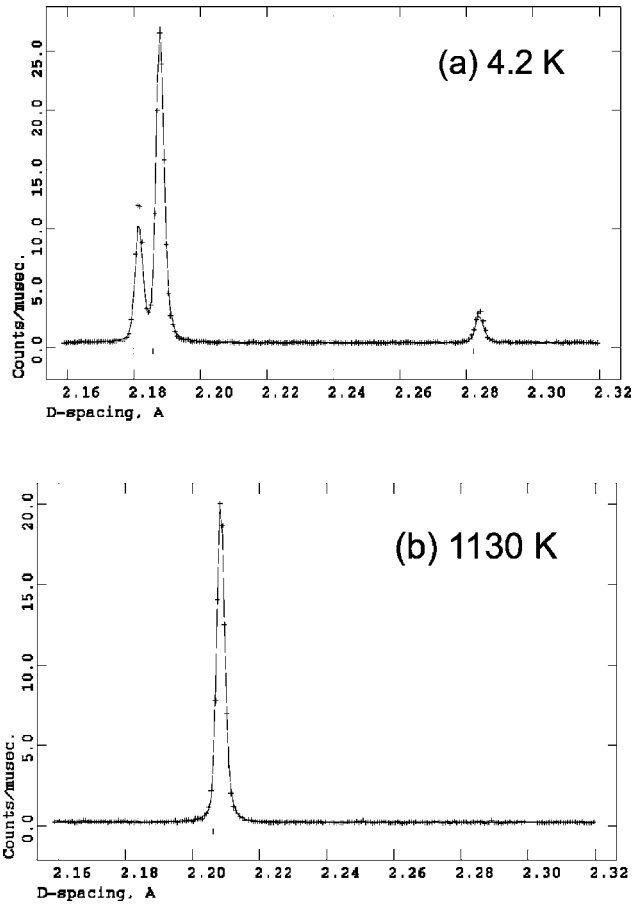

FIG. 4. Parts of the neutron diffraction pattern of $LaAlO_3$ at (a) 4.2 K and (b) 1130 K. These spectra show the splitting of primary peaks (e.g., $d=2.21$ Å; 111 on the cubic P lattice) and superlattice peaks ($d=2.28$ Å; $\frac{3}{2}\frac{1}{2}\frac{1}{2}$ on the cubic P lattice) associated with the rhombohedral phase.

B. Results

Figure 4, showing parts of the diffraction patterns collected at 4.2 and 1130 K, illustrates the two differences between the diffraction patterns of the cubic and rhombohedral phases of $LaAlO_3$. The splitting of diffraction peaks measures the symmetry-breaking spontaneous strain, and the superlattice reflections relate directly to the displacement of oxygen atoms from their sites in the perovskite aristotype structure; in other words, to the rotation of the AlO_6 octahedra around the triad axis.

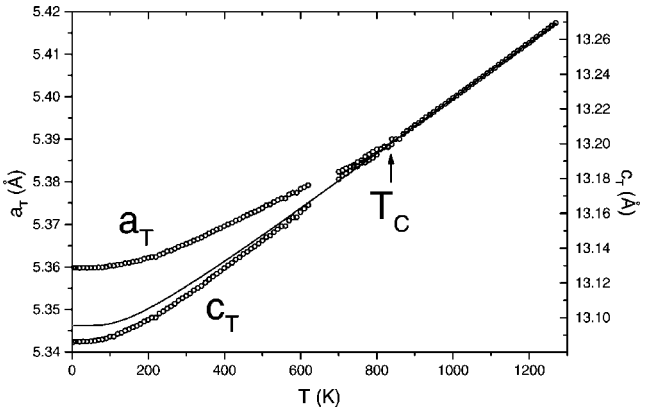

FIG. 5. Refined lattice parameters a_T and c_T for $LaAlO_3$ on the trigonal unit cell; in the cubic phase, $c_T = a_T\sqrt{6}$. The solid line is the baseline behavior of the thermal expansion, in the absence of the phase transition.

Figures 5, 6, and 7 show the raw results of the structure refinements from GSAS; the numerical data are given in Tables I and II. In Fig. 5, the lattice parameters of the trigonal unit cell are shown. On these axes, c is the lattice parameter along the octahedral rotation axis, and a is the lattice parameter in the plane of the octahedral rotation. For the case

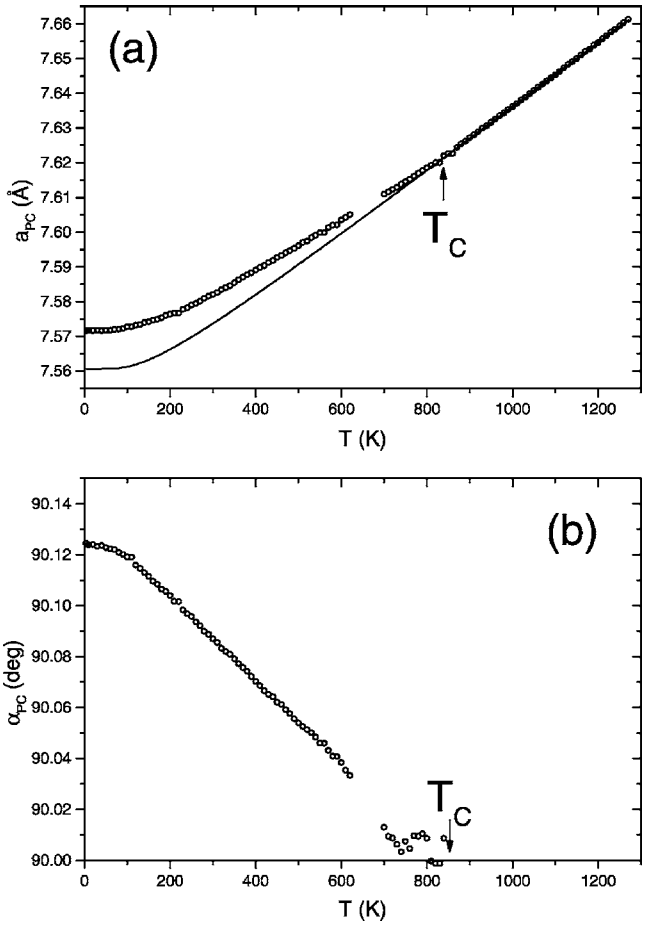

FIG. 6. Refined (a) rhombohedral lattice parameter a_{PC} and (b) lattice angle α_{PC} for $LaAlO_3$ on the pseudocubic unit cell.

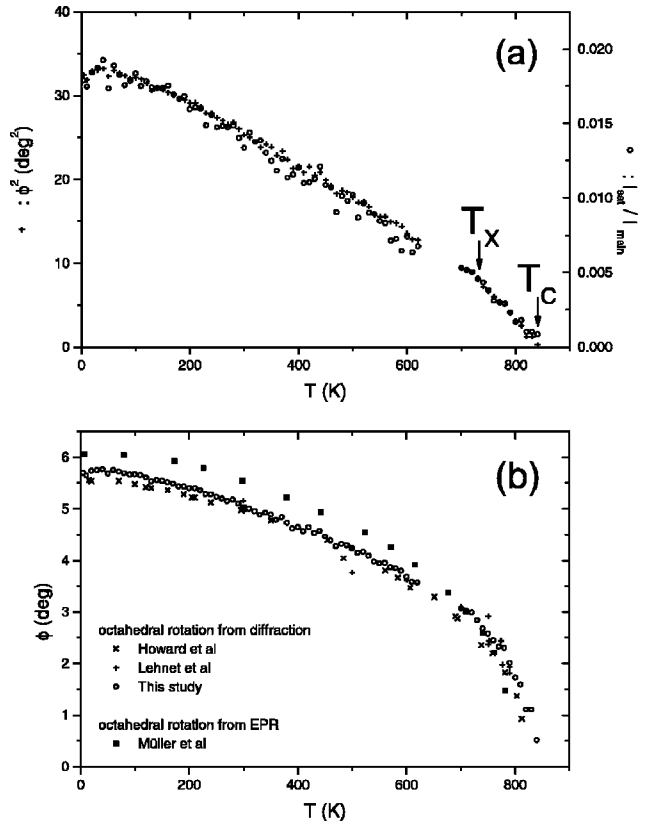

FIG. 7. (a) The intensity of superlattice reflections (such as $\frac{3}{2}\frac{1}{2}\frac{1}{2}$ on the cubic P lattice) relative to the intensity of primary reflections (such as 111 on the cubic P lattice) in the diffraction pattern of $LaAlO_3$ (open circles, right-hand axis) measures the rotation angle of the AlO_6 units (crosses, left-hand axis), according to the relationship $I_{sat} \propto \phi^2$. (b) Comparison of the AlO_6 rotation angle ϕ measured by diffraction experiments by Howard *et al.* (Ref. 10), Lehnert *et al.* (Ref. 12), and this study with data from EPR measured by Müller *et al.* (Ref. 9).

of the AlO_6 octahedra rotating as rigid units, the expected relationships between the trigonal lattice parameters and the rotation angle[32] are

$$a_H = a_{H0} \cos \phi, \tag{4}$$

$$c_H = c_{H0}. \tag{5}$$

These data show two important results. First, the lattice parameter a_T is increased by the phase transition; since pure rotation would reduce a_T, this implies that the AlO_6 octahedra undergo a large degree of stretching in the plane of rotation. Second, the lattice parameter c_T is only slightly affected by the phase transition.

Since changes in a_T and c_T both contribute to the breaking of the cubic symmetry, it is convenient to consider the behavior of the rhombohedral phase on a pseudocubic unit cell (Fig. 6); changes in the lattice parameters a_{PC} and α_{PC} correspond to pure volume changes and pure symmetry-breaking shears, respectively. These data may now be processed in two main ways; by consideration of the

TABLE I. Crystallographic data for rhombohedral $LaAlO_3$. a_T and c_T are the trigonal lattice parameters, a_{PC} and α_{PC} are the pseudocubic lattice parameters. In $R\bar{3}c$ the La occupies the 6*a* sites at 0 0 $\frac{1}{4}$, the Al the 6*b* sites at 0 0 0, and the O the 18*e* sites at *x* 0 $\frac{1}{4}$.

T/K	a_T/Å		c_T/Å		a_{PC}/Å		α_{PC}/(deg)		*x*	
4.2	5.35977	(4)	13.0860	(1)	7.5716	(1)	90.125	(1)	0.5288	(1)
10	5.35981	(6)	13.0863	(1)	7.5717	(1)	90.124	(1)	0.5285	(2)
20	5.35975	(6)	13.0861	(1)	7.5716	(1)	90.124	(1)	0.5290	(2)
30	5.35978	(6)	13.0864	(1)	7.5717	(1)	90.123	(1)	0.5291	(2)
40	5.35975	(6)	13.0862	(1)	7.5717	(1)	90.124	(1)	0.5292	(2)
50	5.35977	(6)	13.0865	(1)	7.5718	(1)	90.123	(1)	0.5287	(2)
60	5.35979	(6)	13.0867	(1)	7.5718	(1)	90.122	(1)	0.5291	(2)
70	5.35991	(6)	13.0871	(1)	7.5720	(1)	90.122	(1)	0.5289	(2)
80	5.35989	(6)	13.0875	(1)	7.5720	(1)	90.121	(1)	0.5288	(2)
90	5.36000	(6)	13.0880	(1)	7.5722	(1)	90.120	(1)	0.5286	(2)
100	5.36029	(6)	13.0890	(1)	7.5727	(1)	90.119	(1)	0.5287	(2)
110	5.36027	(6)	13.0890	(1)	7.5727	(1)	90.119	(1)	0.5286	(2)
120	5.36047	(6)	13.0906	(1)	7.5732	(1)	90.116	(1)	0.5284	(2)
130	5.36057	(6)	13.0913	(1)	7.5734	(1)	90.115	(1)	0.5280	(2)
140	5.36084	(6)	13.0925	(1)	7.5739	(1)	90.113	(1)	0.5281	(2)
150	5.36098	(6)	13.0934	(1)	7.5742	(1)	90.112	(1)	0.5280	(2)
160	5.36118	(6)	13.0945	(1)	7.5746	(1)	90.110	(1)	0.5279	(2)
170	5.36136	(6)	13.0953	(2)	7.5749	(1)	90.108	(1)	0.5277	(2)
180	5.36153	(6)	13.0964	(2)	7.5753	(1)	90.107	(1)	0.5275	(2)
190	5.36195	(6)	13.0978	(2)	7.5760	(1)	90.106	(1)	0.5274	(2)
200	5.36213	(6)	13.0987	(2)	7.5763	(1)	90.104	(1)	0.5273	(2)
210	5.36233	(6)	13.1000	(2)	7.5768	(1)	90.102	(1)	0.5273	(2)
220	5.36232	(6)	13.1000	(2)	7.5767	(1)	90.102	(1)	0.5271	(2)
230	5.36286	(7)	13.1025	(2)	7.5777	(1)	90.098	(1)	0.5267	(2)
240	5.36313	(7)	13.1037	(2)	7.5782	(1)	90.097	(1)	0.5267	(2)
250	5.36366	(6)	13.1053	(2)	7.5790	(1)	90.096	(1)	0.5264	(2)
260	5.36382	(7)	13.1064	(2)	7.5794	(1)	90.094	(1)	0.5263	(2)
270	5.36425	(7)	13.1080	(2)	7.5801	(1)	90.092	(1)	0.5260	(2)
280	5.36475	(7)	13.1100	(2)	7.5810	(1)	90.090	(1)	0.5262	(2)
290	5.36511	(7)	13.1113	(2)	7.5815	(1)	90.089	(1)	0.5258	(2)
300	5.36540	(7)	13.1126	(2)	7.5821	(1)	90.087	(1)	0.5254	(2)
310	5.36574	(7)	13.1139	(2)	7.5826	(1)	90.086	(1)	0.5253	(2)
320	5.36619	(7)	13.1158	(2)	7.5834	(1)	90.083	(1)	0.5250	(2)
330	5.36655	(7)	13.1171	(2)	7.5840	(1)	90.082	(1)	0.5247	(2)
340	5.36689	(7)	13.1183	(2)	7.5846	(1)	90.081	(1)	0.5249	(2)
350	5.36740	(7)	13.1202	(2)	7.5854	(1)	90.079	(1)	0.5247	(2)
360	5.36793	(8)	13.1221	(2)	7.5863	(1)	90.077	(1)	0.5242	(2)
370	5.36837	(8)	13.1237	(2)	7.5870	(1)	90.076	(1)	0.5244	(2)
380	5.36881	(8)	13.1253	(2)	7.5877	(1)	90.074	(1)	0.5239	(2)
390	5.36910	(8)	13.1267	(2)	7.5883	(1)	90.072	(1)	0.5233	(2)
400	5.36959	(8)	13.1286	(2)	7.5891	(1)	90.070	(1)	0.5235	(2)
410	5.37003	(8)	13.1302	(2)	7.5898	(1)	90.069	(1)	0.5230	(2)
420	5.37034	(8)	13.1317	(2)	7.5904	(1)	90.067	(1)	0.5234	(3)
430	5.37087	(8)	13.1335	(2)	7.5912	(1)	90.065	(1)	0.5229	(3)
440	5.37124	(9)	13.1347	(2)	7.5918	(1)	90.064	(1)	0.5231	(3)
450	5.37176	(8)	13.1367	(2)	7.5927	(1)	90.062	(1)	0.5225	(3)
460	5.37216	(9)	13.1380	(2)	7.5933	(1)	90.061	(1)	0.5222	(3)

TABLE I. (*Continued.*)

T/K	a_T/Å		c_T/Å		a_{PC}/Å		α_{PC}/(deg)		x	
470	5.37256	(8)	13.1397	(2)	7.5940	(1)	90.059	(1)	0.5216	(3)
480	5.37291	(9)	13.1410	(2)	7.5946	(1)	90.058	(1)	0.5218	(3)
490	5.37331	(8)	13.1428	(2)	7.5953	(1)	90.056	(1)	0.5217	(3)
500	5.37376	(9)	13.1444	(2)	7.5961	(1)	90.054	(1)	0.5214	(3)
510	5.37438	(9)	13.1464	(2)	7.5970	(1)	90.053	(1)	0.5210	(3)
520	5.37456	(9)	13.1472	(2)	7.5974	(1)	90.051	(1)	0.5210	(3)
530	5.37521	(9)	13.1493	(2)	7.5984	(1)	90.050	(1)	0.5206	(3)
540	5.37563	(9)	13.1509	(3)	7.5991	(1)	90.048	(1)	0.5201	(3)
550	5.37602	(9)	13.1526	(3)	7.5998	(1)	90.046	(1)	0.5199	(3)
560	5.37603	(9)	13.1527	(3)	7.5998	(1)	90.046	(1)	0.5199	(3)
570	5.37696	(9)	13.1559	(3)	7.6013	(1)	90.043	(1)	0.5195	(3)
580	5.37737	(9)	13.1577	(3)	7.6020	(1)	90.041	(1)	0.5194	(3)
590	5.37737	(9)	13.1578	(3)	7.6020	(1)	90.041	(1)	0.5192	(3)
600	5.37827	(9)	13.1608	(3)	7.6035	(1)	90.038	(1)	0.5186	(3)
610	5.37865	(9)	13.1628	(3)	7.6042	(1)	90.035	(1)	0.5181	(3)
620	5.37915	(9)	13.1647	(3)	7.6051	(1)	90.033	(1)	0.5180	(3)
700	5.38233	(11)	13.1795	(4)	7.6109	(1)	90.013	(2)	0.5155	(2)
710	5.38265	(13)	13.1815	(5)	7.6116	(1)	90.009	(2)	0.5153	(2)
720	5.38312	(12)	13.1829	(4)	7.6123	(1)	90.009	(2)	0.5151	(2)
730	5.38342	(15)	13.1845	(6)	7.6129	(1)	90.006	(3)	0.5143	(2)
740	5.38391	(21)	13.1867	(8)	7.6138	(1)	90.003	(4)	0.5135	(2)
750	5.38462	(17)	13.1870	(6)	7.6145	(1)	90.007	(3)	0.5130	(2)
760	5.38499	(17)	13.1889	(6)	7.6152	(1)	90.005	(3)	0.5123	(2)
770	5.38586	(17)	13.1893	(6)	7.6161	(1)	90.010	(3)	0.5118	(2)
780	5.38641	(16)	13.1907	(6)	7.6169	(1)	90.009	(3)	0.5116	(2)
790	5.38703	(17)	13.1919	(6)	7.6177	(1)	90.010	(3)	0.5101	(2)
800	5.38756	(14)	13.1938	(5)	7.6186	(1)	90.009	(2)	0.5087	(3)
810	5.38761	(14)	13.1970	(5)	7.6193	(1)	90.000	(2)	0.5080	(3)
820	5.38808	(14)	13.1985	(5)	7.6200	(1)	89.999	(2)	0.5056	(4)
830	5.38808	(14)	13.1985	(5)	7.6200	(1)	89.999	(2)	0.5056	(4)
840	5.38997	(15)	13.1997	(5)	7.6220	(1)	90.009	(3)	0.5026	(8)

macroscopic spontaneous strains, or by considering the rotation and distortion of the AlO_6 octahedra within the perovskite structure.

The rotation angle for the AlO_6 units is uniquely determined from the structural refinement by the variable x position of the O site, following the relationship[10]

$$\tan \phi = 2\left(x - \frac{1}{2}\right)\sqrt{3}. \tag{6}$$

Figure 7(a) shows the temperature dependence of the AlO_6 rotation angle ϕ. Neglecting thermal effects, the relative intensity of the superlattice reflections is expected to correlate directly to the square of the rotation angle, and this behavior is seen in practice. In Fig. 7(b), we compare the rotation angle observed in this study with other data from the literature.

C. Strain analysis

In the case of a cubic $\leftrightarrow$ pseudocubic rhombohedral phase transition, the spontaneous strain has two components.[4] There is a non-symmetry-breaking strain,

$$e_1 = \frac{a_{PC}}{a_{PC0}} - 1, \tag{7}$$

and a symmetry-breaking strain,

$$e_4 = \left(\frac{a_{PC}}{a_{PC0}} \cos \alpha_{PC}\right), \tag{8}$$

where a_{PC} and α_{PC} are the lattice parameters of the pseudocubic rhombohedral cell, and a_{PC0} is an extrapolation of the behavior of the high-temperature phase to low temperatures [the line in Fig. 6(a)]. The behavior of $a_{PC0}(T)$ is difficult to predict at low temperatures, because of the vanishing of thermal expansion due to quantum mechanical ef-

TABLE II. Crystallographic data for cubic $LaAlO_3$. a is the conventional cubic lattice parameter, a_{PC} is the lattice parameter of the doubled cell (comparable with a_{PC} for the trigonal cell). In $Pm\bar{3}m$ the La occupies the 1b sites at $\frac{1}{2}\ \frac{1}{2}\ \frac{1}{2}$, the Al the 1$a$ sites at 0 0 0, and the O the 3d sites at $\frac{1}{2}$ 0 0.

T/(K)	a/(Å)		a_{PC}/(Å)	
850	3.81130	(3)	7.62261	(6)
860	3.81131	(3)	7.62261	(6)
870	3.81216	(3)	7.62432	(6)
880	3.81269	(3)	7.62538	(6)
890	3.81307	(3)	7.62613	(6)
900	3.81360	(3)	7.62721	(6)
910	3.81400	(4)	7.62800	(7)
920	3.81447	(4)	7.62895	(7)
930	3.81495	(4)	7.62990	(7)
940	3.81534	(4)	7.63068	(7)
950	3.81581	(4)	7.63162	(7)
960	3.81631	(4)	7.63262	(7)
970	3.81675	(4)	7.63349	(7)
980	3.81714	(4)	7.63428	(7)
990	3.81767	(4)	7.63533	(7)
1000	3.81811	(4)	7.63621	(7)
1010	3.81854	(4)	7.63707	(7)
1020	3.81905	(4)	7.63809	(7)
1030	3.81944	(4)	7.63889	(7)
1040	3.81992	(4)	7.63983	(7)
1050	3.82042	(4)	7.64084	(7)
1060	3.82085	(4)	7.64170	(7)
1070	3.82132	(4)	7.64264	(7)
1080	3.82176	(4)	7.64352	(7)
1090	3.82223	(4)	7.64446	(7)
1100	3.82268	(4)	7.64536	(7)
1110	3.82314	(4)	7.64627	(7)
1120	3.82366	(4)	7.64733	(7)
1130	3.82413	(4)	7.64826	(7)
1140	3.82457	(4)	7.64914	(7)
1150	3.82501	(4)	7.65002	(7)
1160	3.82553	(4)	7.65106	(7)
1170	3.82597	(4)	7.65194	(7)
1180	3.82636	(4)	7.65272	(7)
1190	3.82690	(4)	7.65380	(7)
1200	3.82730	(4)	7.65460	(7)
1210	3.82782	(4)	7.65564	(7)
1220	3.82833	(4)	7.65666	(7)
1230	3.82878	(4)	7.65756	(7)
1240	3.82923	(4)	7.65846	(7)
1250	3.82968	(4)	7.65936	(7)
1260	3.83019	(4)	7.66038	(7)
1270	3.83062	(4)	7.66124	(7)

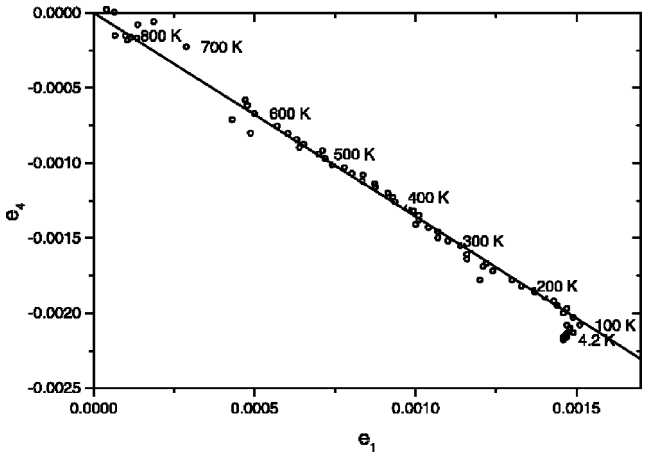

FIG. 8. Plot of e_1 against e_4 in $LaAlO_3$.

fects. Here, $a_{PC0}(T)$ has been fitted to a model with a single quantum mechanical saturation temperature scale.[15] Subtle deviations from this are likely; for example, MgO requires three degrees of saturation to accurately describe its thermal expansion at low temperatures precisely.[30] However, in the absence of concrete data at low temperatures, it is hard to justify the use of additional fitting parameters.

The Landau free energy for a generalized transition from a $Pm\bar{3}m$ perovskite has been determined from symmetry arguments.[31] Using this free-energy expression and the form of the order parameter in a $Pm\bar{3}m \leftrightarrow R\bar{3}c$ transition, the two spontaneous strain components are expected to be proportional to each other, and to Q^2, the square of the order parameter. Figure 8 shows that e_1 and e_4 are indeed proportional over a wide temperature range. The symmetry-breaking strain e_4 is reliably measured in a diffraction experiment when pairs of split diffraction peaks are clearly resolved [such as the 111_{cubic} doublet at 4.2 K in Fig. 4(a)]. Close to T_C, the splitting is smaller, and eventually the two diffraction peaks overlap. The determination of e_4 is then less precise, leading to the scatter seen above 700 K in Fig. 9(b). On the other hand, the non-symmetry-breaking strain e_1 is determined very precisely near T_C, but its measurement becomes less reliable at low temperatures. This is because e_1 depends on the difference between an observed lattice parameter and a baseline extrapolated from high temperatures. Fortunately, there is a reasonably wide temperature range (between 700 K and 400 K, at least, in the case of $LaAlO_3$) where both strain components are determined reliably from the diffraction data. The proportionality observed in this temperature range is most simply explained if both strains vanish at the same critical temperature.

Figure 9 shows the temperature dependence of the two strain components. Both sets of strain data show a small deviation from linear behavior at 730 K. The deviation is rather small, and in the $e_4(T)$ data it is partially masked by the increased scatter in the data in the vicinity of T_C. However, $e_1(T)$ shows a similar nonlinearity, is much less strongly affected by this problem, and is therefore more likely to be accurate.

In perovskites with tilted octahedra, the primary order parameter is conventionally taken to be the rotation angle of

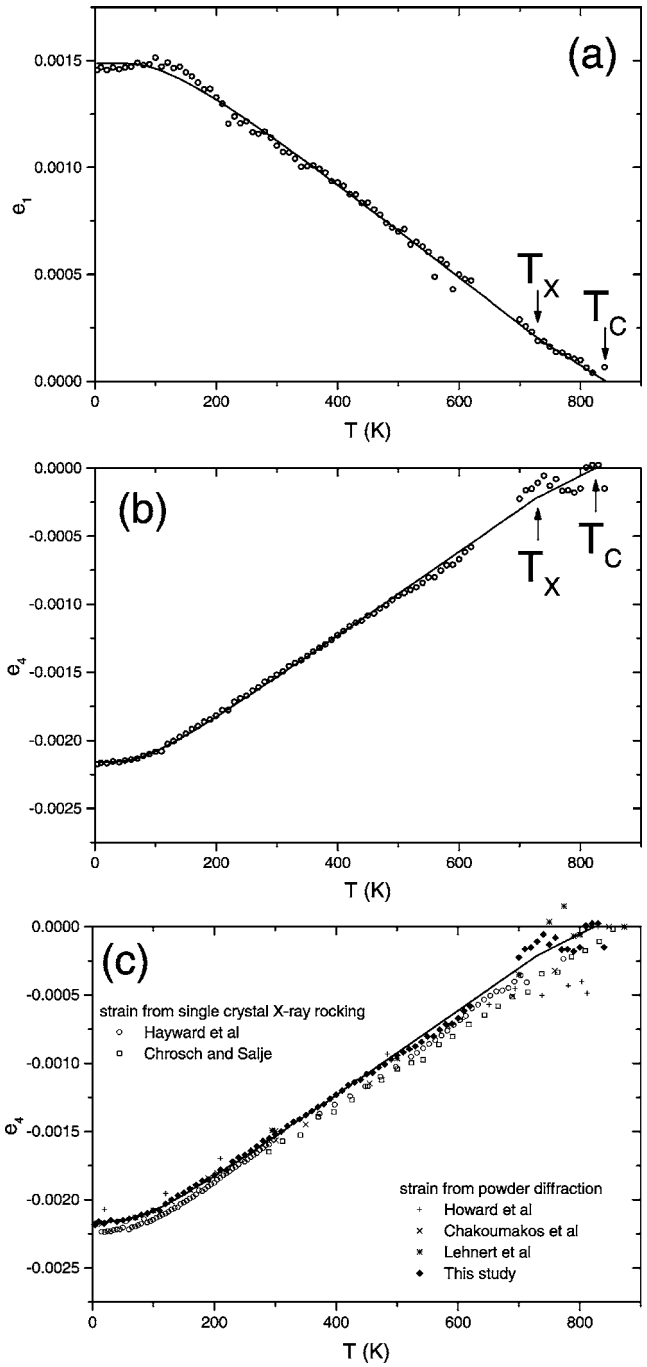

FIG. 9. Spontaneous strains (a) e_1 and (b) e_4 in $LaAlO_3$ as a function of temperature, determined from neutron diffraction data. In each graph, the small break in slope at T_X=730 K is indicated by an arrow. In part (c), the data for e_4 from this study are compared with other data from the literature: these data are from twinned single crystals [Hayward *et al.* (Ref. 15) and Chrosch and Salje (Ref. 14)] and powdered samples [Howard *et al.* (Ref. 10), Chakoumakos *et al.* (Ref. 11), and Lehnert *et al.* (Ref. 12)].

the octahedra. In the case of $LaAlO_3$, this is uniquely determined by the relative intensities of the main and superlattice diffraction peaks, as long as (relatively minor) thermal effects are neglected; this is shown in Fig. 7. Figure 10 shows the variation of the strain component e_4 with the square of

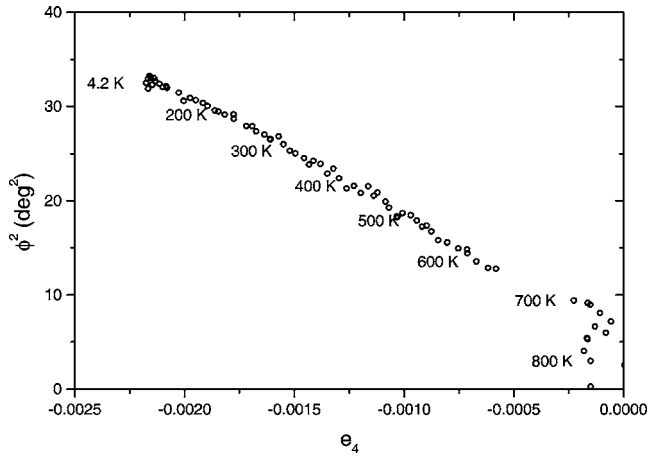

FIG. 10. Relationship between the square of the AlO_6 rotation angle and the symmetry-breaking strain e_4.

the rotation angle. While these quantities are linear with each other over a wide temperature range, they are not proportional. In the raw diffraction data, the main manifestation of this discrepancy is the distinct break in the slope of $I_{sat}(T)$ at 730 K.

D. Rotation and distortion processes

An alternative way of analyzing the same data is to consider the degree to which the AlO_6 octahedra rotate and distort.[6,10,32] Although, in principle, the octahedra could rotate as rigid units, in general, the observed spontaneous strain is not consistent with that expected for the rotation of rigid units. For instance, in the case of the $a^-a^-a^-$ tilt system observed in $LaAlO_3$, the expected spontaneous strains if rigid octahedra rotate through an angle ϕ (in radians) are

$$e_1 = \frac{-\phi^2}{3}, \quad e_4 = \frac{\phi^2}{3}, \tag{9}$$

which, given ϕ=5.7°=0.099 radians at 4.2 K, would imply e_1=−0.0033, and e_4=0.0033. The observed strains have the opposite signs to these, and substantially smaller magnitudes. This discrepancy is explained by the distortion of the octahedra as they rotate.

In $a^-a^-a^-$ perovskites, it is found empirically that the octahedra are flattened down their rotation axis.[10] This deformation is quantified by a shape factor $(1-\eta)$, where η is the ratio of the lengths of the octahedron parallel and perpendicular to the triad axis. The shape factor $(1-\eta)$ is 0 in a regular octahedron, and greater than 0 in an octahedron compressed down the triad axis. Further discussion of this point is given elsewhere[6,32] using a slightly different notation. The distortion of octahedra has been analyzed using the Landau theory by Darlington,[6] who concluded that the shape factor of the octahedra, $(1-\eta)$, should be proportional to the square of the octahedral rotation. Using the discrepancy between the observed spontaneous strain e_4 and the value predicted for rigid body rotation, the octahedral shape factor $(1-\eta)$ was determined from each powder-diffraction refinement. Its temperature dependence is shown

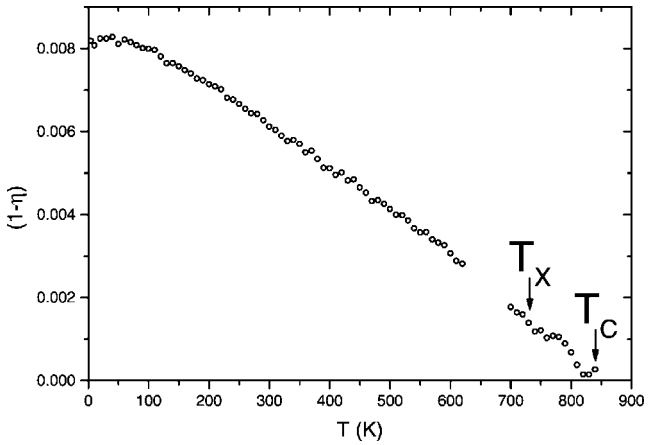

FIG. 11. Temperature dependence of the octahedral distortion factor $(1-\eta)$ in $LaAlO_3$.

in Fig. 11, and the relationship between ϕ^2 and $(1-\eta)$ is shown in Fig. 12.

III. DIELECTRIC RELAXATION

Dielectric measurements were carried out on a $LaAlO_3$ single crystal with sputtered platinum electrodes using impedance spectroscopy. The platinum electrodes were annealed at 675 K prior to measurement. Measurements were carried out between room temperature and 1000 K over the frequency range 5 Hz–13 MHz using an HP4192A impedance analyzer.

At temperatures below ~550 K, the sample conductivity was too low to be measured with the apparatus described. At higher temperatures, two relaxations were observed in the impedance spectra, as indicated by two semicircular arcs in the impedance complex plane plot as shown at various temperatures in Fig. 13(a). The high-frequency relaxation, represented by the arc nearest the origin had an associated capacitance of 2.25 pF cm^{-1} which was largely independent of

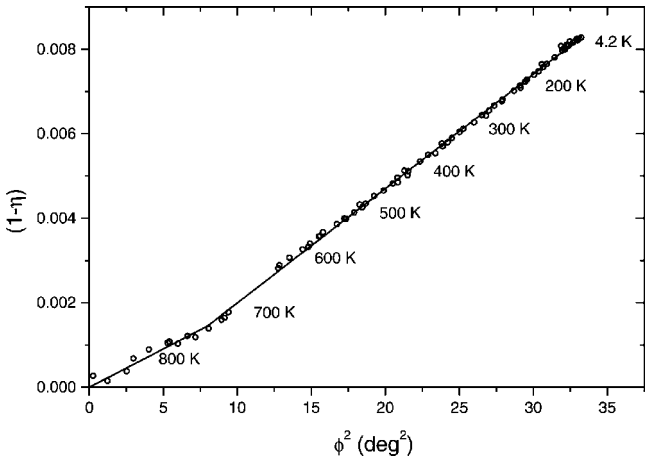

FIG. 12. Variation of the octahedral distortion factor $(1-\eta)$ with the square of the octahedral rotation angle ϕ^2 in $LaAlO_3$. If the phase transition were driven by a single order parameter in a Landau-type system, these quantities should be proportional.

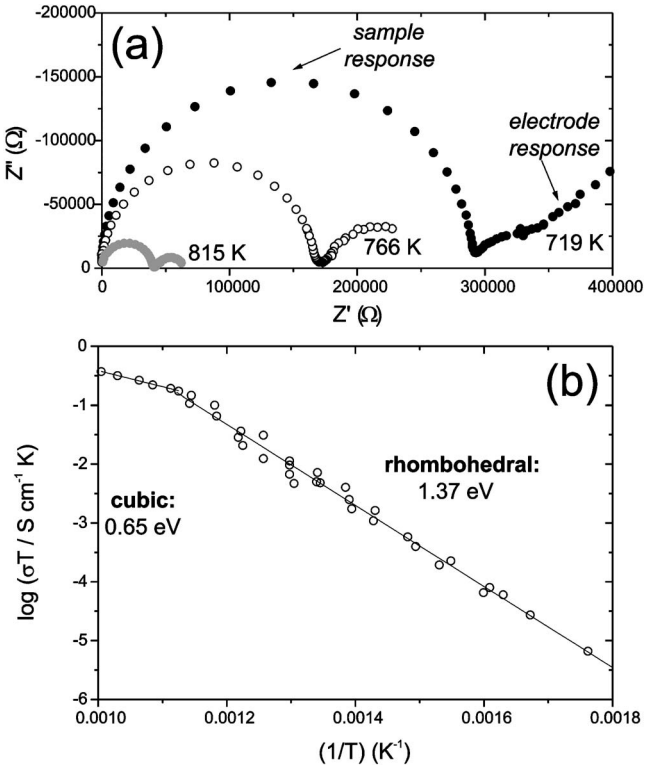

FIG. 13. Selected impedance data at various temperatures, displayed (a) in the complex plane, and (b) as an Arrhenius plot of conductivity in a bulk $LaAlO_3$ single crystal.

temperature; this capacitance corresponds to a permittivity of $\varepsilon' = 25$ and is in good agreement with the data of Cho *et al.*[33] for that of $LaAlO_3$. This response was therefore attributed to that of the bulk $LaAlO_3$ crystal. The second, low-frequency response had an associated capacitance of the order 0.2 μF cm^{-1} across the temperature range studied, a value consistent with an electrode response.[34] Conductivity data for bulk $LaAlO_3$ were extracted from the intercept of the semicircular arc in the impedance complex plane plot over the temperature range 550–1000 K [Fig. 13(a)] and are presented in an Arrhenius plot in Fig. 13(b). The data clearly show two distinct areas of linear behavior. Below 843 K, conduction is dominated by a process with an activation energy of ~1.37 eV. This value is consistent with that observed for oxygen ion conduction in Sr-doped $LaAlO_3$.[35] In the cubic polymorph (above 843 K) the activation energy decreases to ~0.65 eV. This drop in activation energy associated with the structural transformation was also observed previously[35] and was explained by easier migration by oxygen through the nondistorted octahedra of the cubic system. An alternative mechanism is associated with the deeper trapping sites generally afforded by twin boundaries in distorted perovskites.[36]

The origin of the oxygen vacancies causing this conductivity in the undoped crystal is not immediately clear. Oxygen vacancies are most likely to be present as compensating defects for impurity acceptor states, which are common in perovskite oxides. Alternatively, they may arise from Schottky disorder associated with the high-temperature growth conditions used in the manufacture of the crystals; in

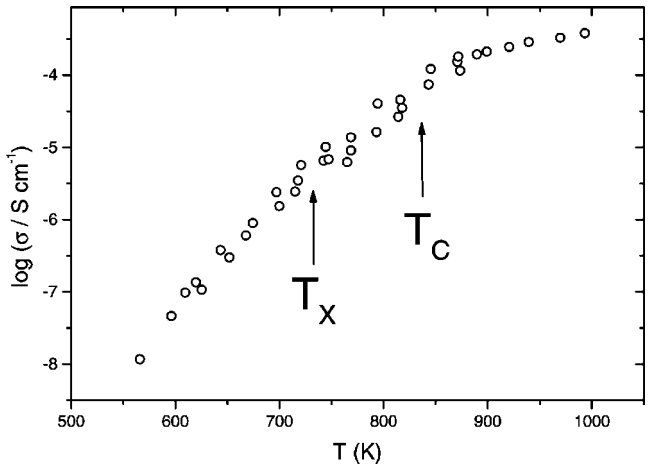

FIG. 14. Plot of conductivity as a function of temperature in a bulk $LaAlO_3$ single crystal indicating the dramatic increase in oxygen vacancy motion below the phase transition.

this instance it is unlikely that the associated La and Al vacancies would contribute significantly to the conductivity. In Fig. 14 we replot the conductivity data versus T rather than $1/T$; this is to demonstrate clearly that the conduction rises exponentially by four or five orders of magnitude over a range of temperature ~300 K below the transition temperature and that this increase is not closely associated with transition dynamics. Note, in particular, the implication that although there is no static structural phase transition below the rhombohedral-cubic transformation, dynamic measurements on time scales that are long compared with the characteristic relaxation time may manifest a different time-averaged local symmetry. By using the known oxygen vacancy ionic mobility at 293 K and its known temperature dependence in the cubic perovskite phase of $(Ba,Sr)TiO_3$ of $\mu=2\times10^{-12}$ cm^2 V^{-1} s^{-1},[37] we can estimate the concentration of oxygen vacancies at the cubic phase transition temperature as $\sim10^{19}$ cm^{-3}.

It is interesting to compare dielectric data (in the MHz regime) with mechanical data in the Hz regime.[38] In the simplest case the response over six decades of frequency would be dominated by a single relaxation process. Figure 15 shows that this is indeed the case, where the data over a wide range of temperatures satisfy a textbooklike single relaxation mechanism.

IV. CALORIMETRY

The sample used in the calorimetry experiments was a polished 1-mm-thick section, grown by the Czochralski method by Crystal Gmbh (Berlin). To improve thermal contact, the sample was coated in platinum; the same sample had previously been used for the dielectric measurements described in Sec. III. Specific-heat measurements were performed using a Perkin-Elmer "Diamond" calorimeter, operating in the conventional (but fast) scanning mode, with a heating rate of 500 K min^{-1}. Heat flow data were normalized against a sapphire standard, and the resulting C_P data are shown in Fig. 16.

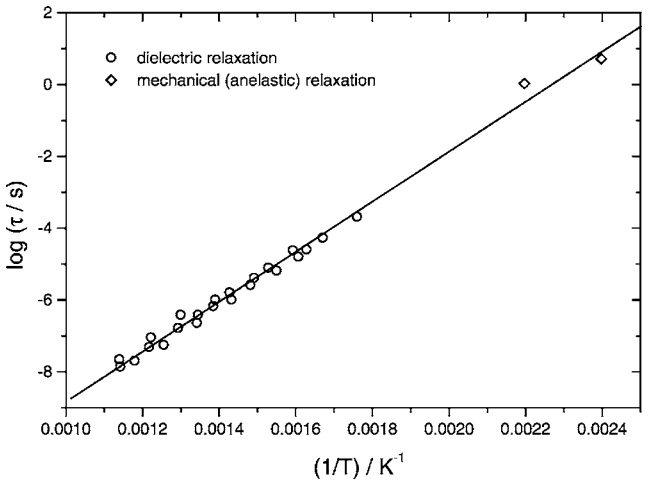

FIG. 15. Arrhenius plot of relaxation time measured mechanically and via dielectric response; a single activation energy characterizes the process over nine decades of time. Mechanical relaxation data are from Ref. 38.

The baseline was determined using an Einstein model, with an empirical linear correction for the thermal expansion of the sample

$$C_P = 3nR\left(\frac{\theta_E}{T}\right)^2 \frac{\exp(\theta_E/T)}{[\exp(\theta_E/T)-1]^2} + \alpha T. \qquad (10)$$

The free parameters in this model, θ_E and α, were fitted by assuming that $\Delta C_P=0$ above the transition ($T>860$ K) and also substantially below the transition ($T<400$ K). While the second of these conditions is not strictly correct, it does not affect the baseline in the vicinity of T_C very much. These specific-heat data show a second order step at 813 K, with $\Delta C_P=0.103$ J K^{-1} g^{-1}=21.939 J K^{-1} mol^{-1}, essentially agreeing with the results of Bueble *et al.*[13] Both data sets have a small peak superimposed on the Landau step and a tail above the transition temperature. Compared to the specific-heat anomalies observed for polyhedral tilting tran-

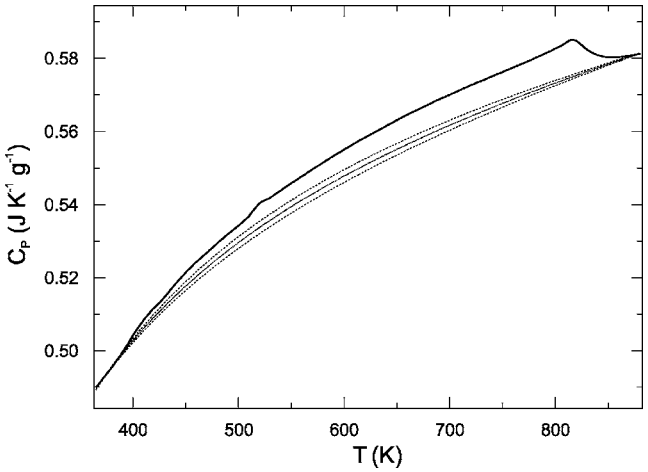

FIG. 16. Specific heat of $LaAlO_3$. The solid line is the experimental data; the dashed line shows the best-fit baseline, and the dotted lines to either side of this show the 95% confidence limits.

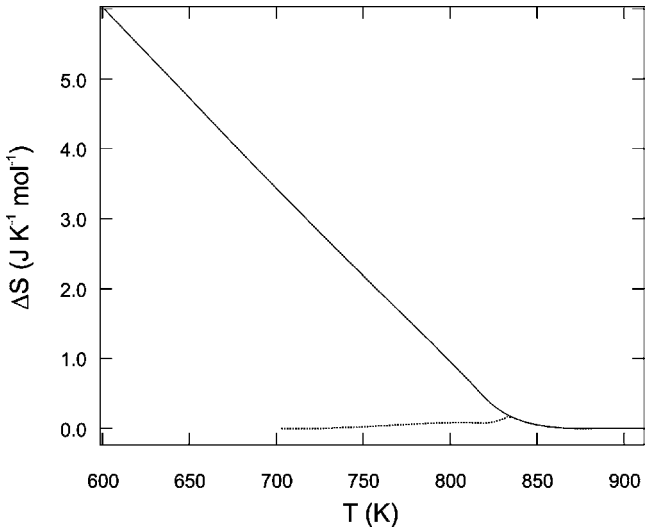

FIG. 17. Excess entropy in $LaAlO_3$. The solid line shows the calculated $-\Delta S$; the broken line shows the deviation from linearity just below T_C.

sitions in tetragonal perovskites, such as $SrTiO_3$,[23] this is rather large.

We obtain the excess entropy for the transition by integrating $(-\Delta C_P/T)dT$, leading to the entropy vs temperature graph shown in Fig. 17. While these data are mostly linear with (T_C-T), consistent with a second-order Landau phase transition, there is a small deviation from linearity; this excess is shown by the broken line in Fig. 17.

V. BIREFRINGENCE

The birefringence and domain structure of $LaAlO_3$ were studied simultaneously using the rotating analyzer imaging method,[39] as implemented in the Metripol birefringence microscope (Oxford Cryosystems). By using a charge-coupled device (CCD) camera to record the intensity transmitted through the optical chain described by Glazer *et al.*[39] and Geday and Glazer[40] it is possible to record the birefringence, optical orientation and absorption as a function of position. Each of these quantities can be displayed as a false-color map; the birefringence map is analogous to the image obtained by looking at a sample between crossed polarizers with white light, albeit with different relationships between color and retardation.

Colorless sections of $LaAlO_3$ 100-μm-thick were cut parallel to (100) and (110) on the cubic axes and placed in a Linkham heating stage. Both samples were twinned, reflecting the e_4 strain seen in $LaAlO_3$. The crystals were heated at 1 K per minute from 93 to 873 K. This heating rate allowed maps of transmitted intensity, birefringence, and optical orientation to be recorded at 0.5 K intervals.

To determine the quantitative variation of the birefringence with temperature, a small box (around 15×15 pixels, or 0.03 mm$\times$0.03 mm) was selected in each set of images, and the birefringence in these 225 pixels was averaged. In the (110) slice, which has no visible twins, this process was routine and could be performed automatically. For the (100) slice, however, the domain structure was more complex and mobile. For this reason, the position of the box had to be carefully chosen to not cross any domain boundaries and to correct for the sample or domain movement. To achieve this, a single, clearly recognizable twin domain was identified, and the averaging box was placed manually in the center of this domain for each image.

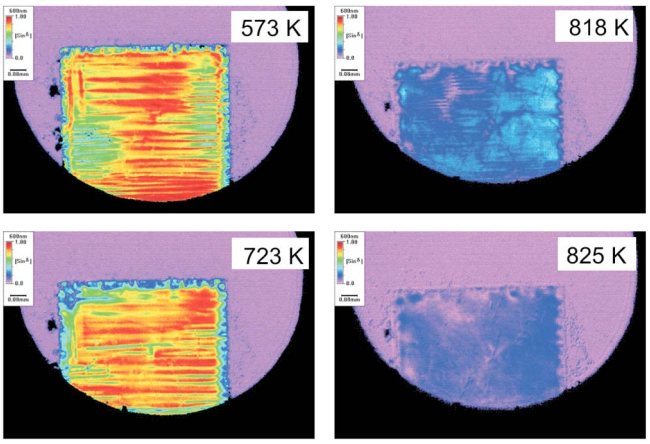

FIG. 18. (Color online) Birefringence maps for a (100) slice of $LaAlO_3$ at four temperatures. The scale bar is 0.08 mm.

A. (100) slice

Representative birefringence maps for the (100) slice are shown in Fig. 18, and Fig. 19 is a graph of the retardation as a function of temperature. These data agree well with the relationship $\Delta n \propto \phi^2$.

At 818 K (top right), the sample is still birefringent and still has definite twin domains. However, by 825 K (bottom right), the twin domains appear to have vanished, even though the sample is still anisotropic. This seems to indicate that the transition temperature is 830 K, but that the twin walls only appear below around 820 K.

B. (110) slice

Since $LaAlO_3$ is rhombohedral at low temperatures, it is optically uniaxial. Consequently, measurements of the bire-

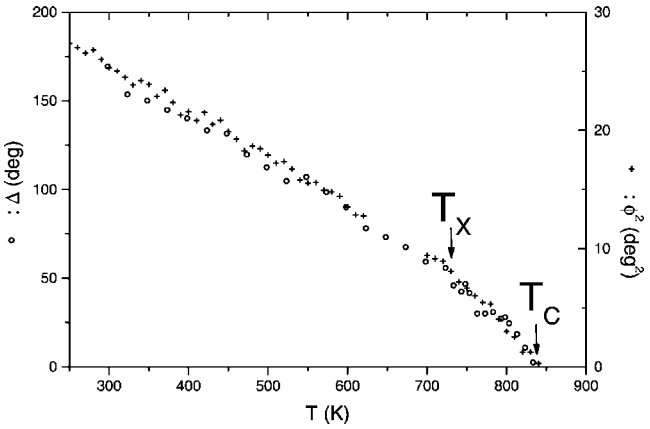

FIG. 19. Temperature dependence of the optical retardation of a (100) slice of $LaAlO_3$ (open circles, left-hand axis). These data show the same behavior as the square of the AlO_6 rotation angle, as measured by neutron diffraction (crosses, right-hand axis).

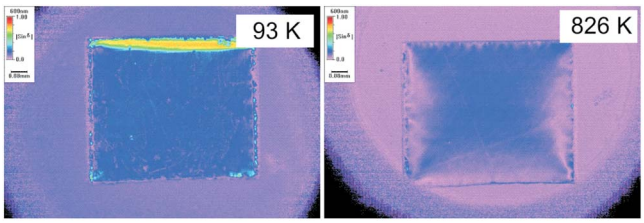

FIG. 20. (Color online) Birefringence maps for a (110) slice of $LaAlO_3$, at two temperatures. The scale bar is 0.08 mm.

fringence made in differently oriented sections are expected to be proportional to each other. A sample cut along the (110) plane had no visible twins at any temperature, as shown in Fig. 20. Just below 830 K (the measured T_C in this apparatus), substantial strain fields develop around the edges of the crystal.

The graph of Δ versus temperature is shown in Fig. 21. As for the (100) slice, the birefringence vanishes at $T_C=830$ K. The low-temperature data extrapolate to zero at a higher temperature than T_C, similar to the behavior seen for the birefringence of the (100) slice. However, the deviation from linearity between 830 K and 750 K has a markedly different form, including a peak in Δ at 820 K.

The origin of this peak may be understood by considering the images of the (100) slice in Fig. 18 above. The (110) slice has no visible twins, but may be twinned parallel to the sample's principal face. The retardation data between 830 K and 820 K are apparently for a monodomain sample, which then develops twins at lower temperatures. Around 800 K, domains in length fast and length slow orientations approximately cancel, so that the net birefringence of the sample is nearly zero. Below 750 K, the domain structure appears to be quite stable, which is consistent with the direct imaging of the domains in Fig. 18. In this situation, the overall retardation of the sample is proportional to the sample birefringence, and so Δ is a correct measurement of Q^2.

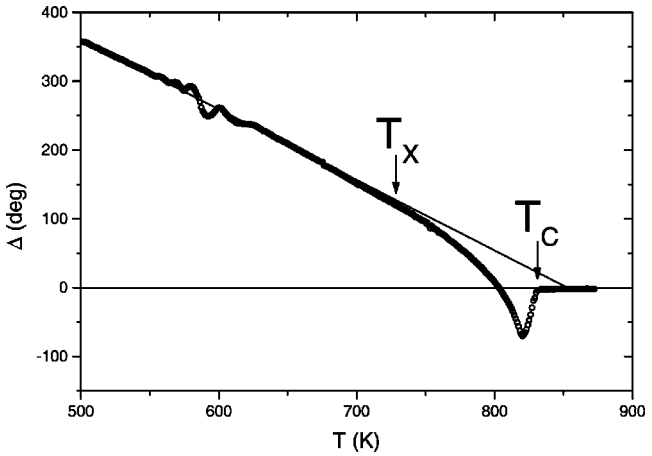

FIG. 21. Temperature dependence of the optical retardation of a (110) slice of $LaAlO_3$. The line is a best-fit line to data in the temperature range $T<700$ K. The noise around $T=575$ K, $\Delta=270°$ is an artifact of the data analysis.

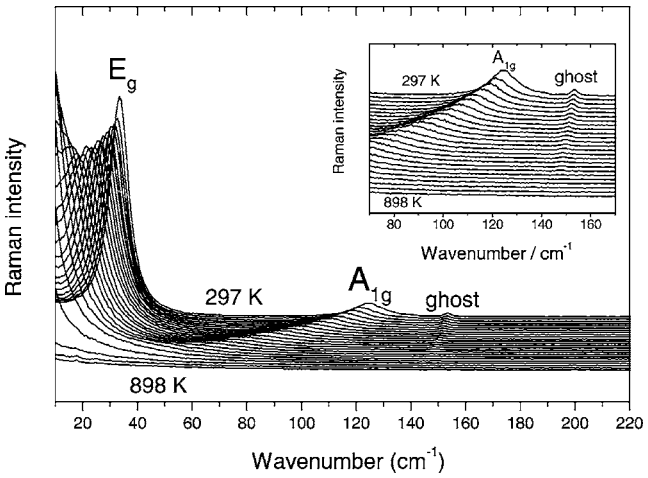

FIG. 22. Raman spectra of $LaAlO_3$ as a function of temperature from room temperature to above the transition temperature. The inset graph shows the weak A_{1g} mode with an enhanced intensity scale.

VI. RAMAN SPECTROSCOPY

The lattice dynamics of the phase transition in $LaAlO_3$ are described by Abrashev *et al.*[41] The soft mode in the cubic phase has F_{2u} symmetry and is threefold degenerate; it splits into $1A_{1g}$ and $2E_g$ modes in the rhombohedral phase. These modes are only Raman active, and both represent rotations of the AlO_6 octahedra. Given the degeneracy of the E_g modes, these modes correspond to the behavior of the structure in the plane perpendicular to the rotation axis, and the A_{1g} mode to the behavior along this axis. In each case, the soft mode frequency is proportional to the inverse susceptibility. In addition, a number of "ghost" modes have been observed in $LaAlO_3$;[16,41] the most important of these (at 152 cm^{-1}) has also been observed in $NdAlO_3$.[16]

Raman spectra between 4 cm^{-1} and 665 cm^{-1} were recorded in a backscattering with a T64000 Jobin-Yvon ISA multichannel triple monochromator Raman spectrometer equipped with an Olympus FX40 microscope (long-working-distance objective $\times 50$) and a liquid-nitrogen-cooled CCD detector. The measurements were done with gratings of 1800 lines per mm and the laser line of 514.5 nm (power 100 mW) excitation of a coherent argon-krypton ion laser. The calibration of the Raman shift was confirmed by reference to silicon and diamond standards. The sample heating and cooling was carried out using standard heating-cooling stages. The Raman spectra at various temperatures are shown in Fig. 22.

The soft mode frequencies were determined by fitting the peaks shown in Fig. 22, taking account of damping effects, with the results shown in Fig. 23. The E_g mode frequency could not be determined close to T_C, since the E_g peak is lost in the Raleigh line. The extrapolation of the A_{1g} mode to zero frequency [Fig. 23(a)] gives $T_C=806$ K. Similar extrapolation of the E_g mode frequency [Fig. 23(b)] would see the mode softening at 763 K. Since the T_C values for the two modes are derived from the same raw spectra, this difference cannot be due to problems of temperature calibration.

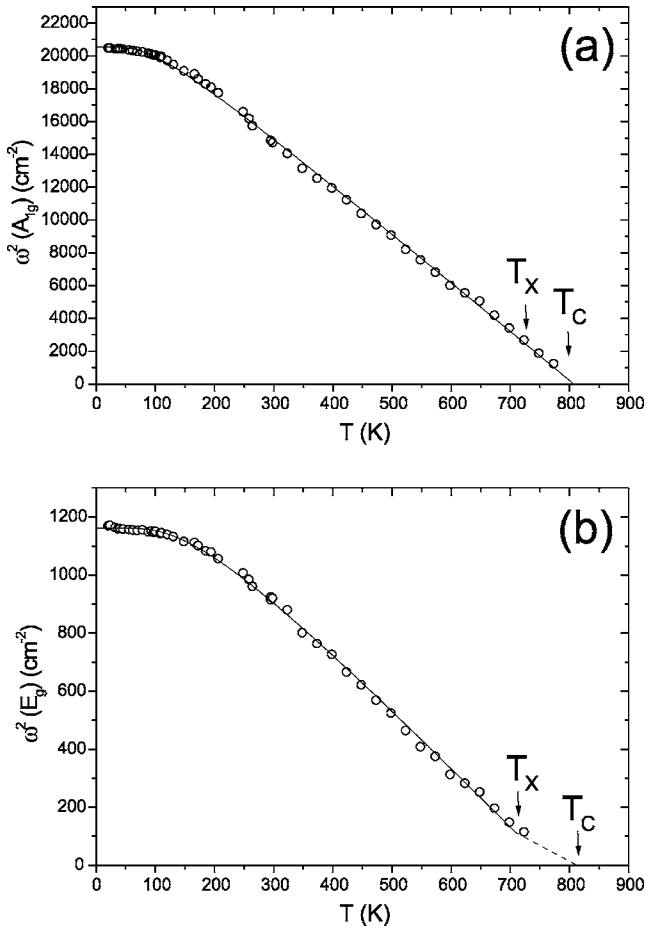

FIG. 23. Temperature dependence of soft mode frequencies in $LaAlO_3$. In (b), the solid line is a best fit to a quantum mechanical Landau model for data in the range $T<690$ K. The broken line shows a more speculative best fit through data for $T<690$ K.

Another way of considering the same phenomenon is to plot the mode frequencies against each other, as in Fig. 24. For the A_{1g} and E_g modes to soften at the same temperature, there must be some deviation from the linear model illustrated by the solid line in Fig. 24. In all the other experiments reported here, there are anomalies in the data approximately 100 K below the transition temperature. The impossibility of measuring the E_g mode frequency so close to T_C prevents this effect being studied in detail from the Raman data. The broken line in Figs. 23(b) and 24 show how the E_g mode would have to behave for the two modes to have the same transition temperature. While the data are ambiguous, it is worth noting that a line through the two highest-temperature points on the $\omega^2(A_{1g})$ vs $\omega^2(E_g)$ graph passes through the origin. This is the behavior expected when both mode frequencies depend on the same order parameter susceptibility and not the behavior observed at lower temperatures. The crossover temperature measured in the Raman experiment is approximately 710 K, which is 100 K below the transition temperature observed in the A_{1g} mode softening.

The qualitative forms of the $\omega^2(T)$ graphs for the two soft modes are consistent with the structural behavior seen in Sec. II above. Projected onto the triad axis, the structure is essentially invariant across the phase transition; the spontaneous strain along this axis is negligible. This agrees with the observation that the A_{1g} soft mode has a high frequency and, hence, corresponds to a low susceptibility; the soft mode along the rotation axis is rather stiff. Perpendicular to the rotation axis, there are more significant structural changes (manifest in both the spontaneous strain and the octahedral rotation and distortion), with an anomaly approximately 100 K below the transition temperature. These results match the Raman data for the E_g soft mode, which has a lower frequency than the A_{1g} mode, though with an apparent hardening near T_C-100 K.

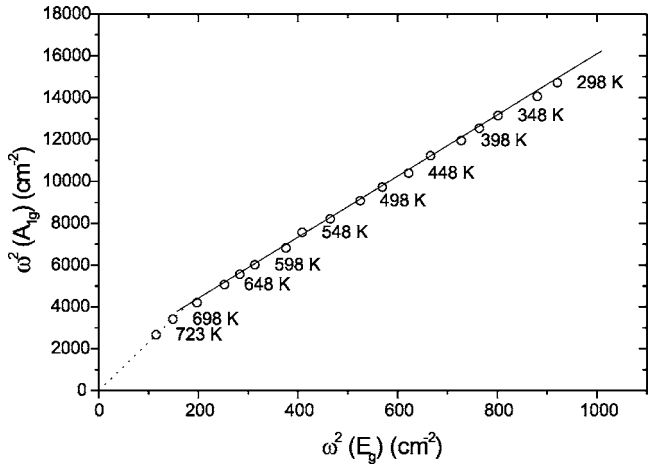

FIG. 24. Mutual variation of soft mode frequencies in $LaAlO_3$, showing a slight deviation from proportionality in the measured data. The solid line is a best fit to data for 300 K$<T<$690 K. The broken line shows a more speculative best fit through data for $T<690$ K.

VII. DISCUSSION

A. Synthesis of data

In this study, we have studied the structural behavior of the improper ferroelastic $LaAlO_3$ by a number of methods. The most important anomaly in each experiment is associated with the cubic-rhombohedral phase transition. The discrepancies in the measured transition temperatures almost certainly arise from slight differences between the temperature calibrations of the various experiments; the most reliable transition temperature is from calorimetry, which gave $T_C=813$ K. It is interesting that the onset of macroscopic twinning in this system, as evidenced by the birefringence imaging and measurement, occurs approximately 10 K below the transition temperature.

Many of the data show a second, weaker anomaly approximately 100 K below T_C. There are changes in the temperature dependence of the AlO_6 rotation angle and distortion factor, and there is evidence for an anomaly in the spontaneous strain. Similar behavior is seen for the birefringence. In addition, the twin microstructure is stable below this crossover temperature, but rather mobile above it.

In the Introduction, it was noted that the behavior of $LaAlO_3$ below the transition temperature does not conform to a second-order Landau model with a single-order param-

eter, though it was not clear from the existing data what the quantitative form of this deviation was, making it difficult to determine its physical origin. From the neutron diffraction measurements of ϕ^2 (or I_{sat}) in Sec. II, it is apparent that the form of the $Q^2(T)$ graph is linear from T_C to approximately 100 K below T_C. There is then a pronounced kink. At lower temperatures, the $Q^2(T)$ graph is also linear, though with a different gradient to the high-temperature regime. The result $Q^2 \propto |T_C - T|$ seen near T_C implies that nonclassical criticalities[9] are not the origin of the 730 K anomaly in $LaAlO_3$. The sharpness of the kink in $Q^2(T)$ is not consistent with the 730 K anomaly being caused by quantum mechanical effects,[15] which would lead to a more gradual deviation.

Comparing the data for the order parameter with those for the spontaneous strains e_1 and e_4 indicates that the predictions of classical coupling theory do apply, but only in the temperature range 730 K $< T < T_C$. Below this temperature, the relationship between ϕ, η, and e_S is modified. In the context of mean field theory, this may be explained by biquadratic coupling to another process.[21] From the conductivity measurements and birefringence imaging of the two domains, this second process appears to be linked to the oxygen vacancy mobility. Conductivity measures this mobility directly, but the twin microstructure (measured in this study by birefringence imaging) is also influenced by the mobility of oxygen vacancies. Where this is low, the vacancies pin the twin domains, leading to a stable microstructure. As the vacancies become more mobile, the pinning effect is reduced, and the domain walls become more mobile. This is seen both directly in images of $LaAlO_3$ crystals, and in the behavior of the optical retardation of a (110) slice of $LaAlO_3$ containing some (110) twins in Fig. 21.

One model would be that the oxygen vacancies are essentially static and clustered below 730 K and dynamically disordered above 730 K. Locally clustered vacancies [analogous to those seen in $BaTiO_3$ (Ref. 42) and $CaFe_xTi_{1-x}O_{3-x/2}$ (Ref. 43)] would be expected to pin twin walls quite effectively, even at concentrations in the parts-per-thousand to parts-per-million range. Electron microscopy studies[44] on $BaTiO_3$ have shown pronounced collection of oxygen vacancies on twin walls. Since the order parameter is oxygen octahedron rotation, the influence of oxygen vacancies on the order parameter should be strong; moreover, oxygen vacancies will influence strain relaxation coupled to this order parameter. For instance, in $SrTiO_3$ an oxygen vacancy concentration of the order 10^{20} cm^{-3} (corresponding to a bulk composition $SrTiO_{2.998}$) reduces the ferroelastic transition temperature from 105 to 80 K.[45]

This coupling anomaly is the origin of the large apparent θ_S values obtained for the order parameter in various studies, as noted previously;[15] the simple model in Eq. (1) will overestimate θ_S to attempt to fit the kink seen in Fig. 7. If only data below the 730 K anomaly are fitted, $\theta_S = 150(7)$ K for the rotation angle data, and 137(7) K for the distortion data, then the θ_S values agree within error. These fits are shown in Fig. 25.

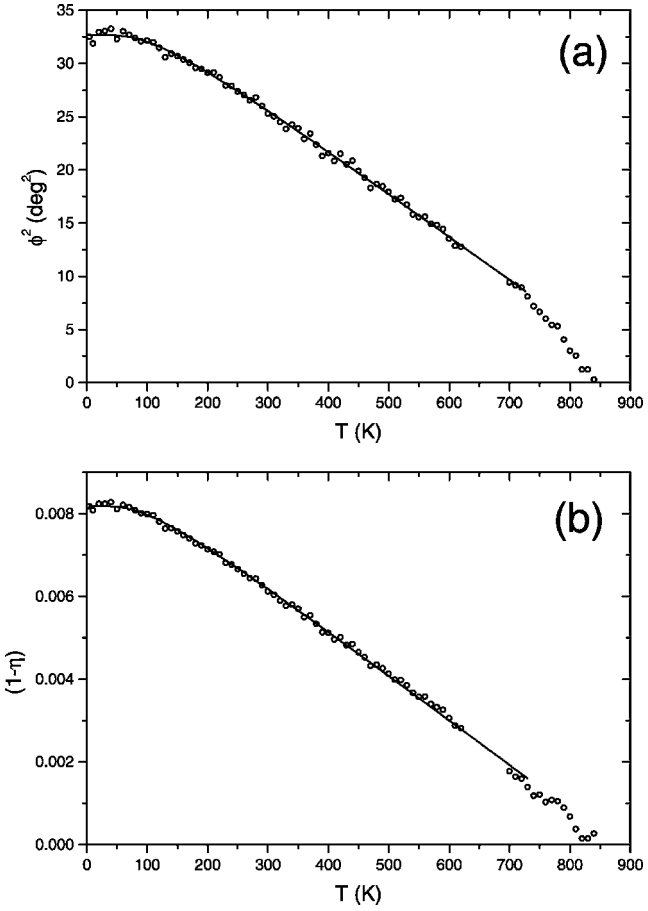

FIG. 25. Temperature dependence of the (a) AlO_6 rotation and (b) AlO_6 distortion in $LaAlO_3$. The fits are to Landau models with quantum mechanical saturation, fitting data for the temperature range $T < 730$ K.

B. Landau theory

If we consider experimental data such as the AlO_6 rotation angle, the temperature dependence of the order parameter is given by $\phi(T) \propto (T_C - T)^{1/2}$, which is classical second-order Landau behavior. Around 730 K, this behavior is modified; while $\phi^2(T)$ is still linear, it has a different gradient at lower temperatures. This behavior is consistent with biquadratic coupling between the rotation angle and another process.[21] The Landau potential for the simplest case (two second-order transitions) would have the form

$$G = \frac{A_1}{2}(T - T_{C1})Q_1^2 + \frac{B_1}{4}Q_1^4 + \frac{A_2}{2}(T - T_{C2})Q_2^2 + \frac{B_2}{4}Q_2^4 + \lambda Q_1^2 Q_2^2. \quad (10')$$

The equilibrium condition $\delta G / \delta Q = 0$ leads to three types of solution[1]

$$\text{(I)}: Q_1 = Q_2 = 0 \quad (11)$$

$$\text{(II)}: Q_1^2 = \frac{B_1}{A_1}(T_{C1} - T), \quad Q_2 = 0 \quad (12)$$

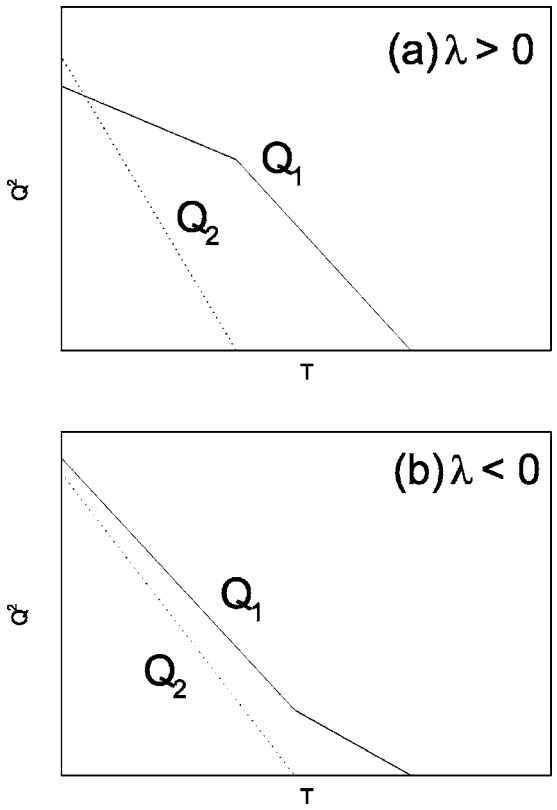

FIG. 26. Temperature dependence of two order parameters with biquadratic coupling, where the coupling (a) hinders and (b) favors the mixed phase.

$$(\mathrm{III}):\ Q_1^2 = \frac{A_1B_2(T_{C1}-T) - 2\lambda A_2(T_{C2}-T)}{B_1B_2 - 4\lambda^2}, \qquad (13)$$

with an equivalent solution for Q_2^2.

The precise form of the variation of Q_1 and Q_2 depends on the strength of the coupling constant λ. For small values of λ, the sequence of phases observed on cooling is I-II-III, with a change in the gradient of ${Q_1}^2(T)$ at T_X. If we label the order parameter with the higher critical temperature Q_1, then for negative λ (the mixed phase is favored), the crossover temperature will be higher than T_{C2}, and ${Q_1}^2$ will increase more rapidly with T in phase III than in phase II

$$T_X = \frac{B_1A_2T_{C2} - 2\lambda A_1T_{C1}}{B_1A_2 - 2\lambda A_1}. \qquad (14)$$

Conversely, for positive λ, the crossover temperature will be lower than T_{C2}, and ${Q_1}^2$ will increase more slowly with T in phase III than in phase II. These possibilities are shown in Fig. 26.

Comparison of these models with the observed behavior of the order parameter ϕ in $LaAlO_3$ indicates that the second process implies that the coupling between the ferroelastic transition and the second process—postulated to be oxygen vacancy clustering—is unfavorable. On cooling, the onset of oxygen vacancy clustering hinders the further increase in the AlO_6 rotation angle.

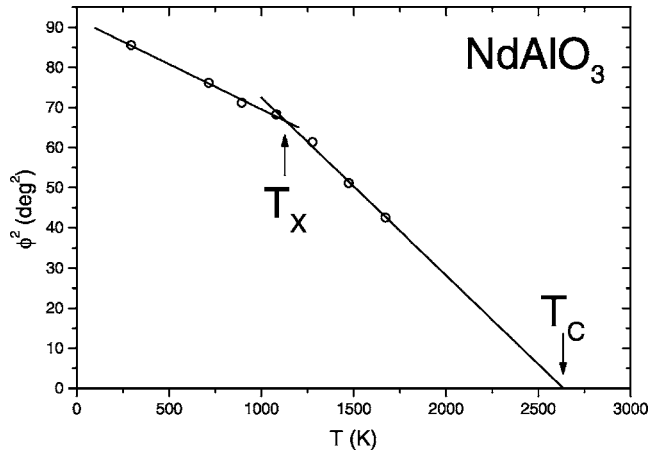

FIG. 27. Temperature dependence of the square of the AlO_6 rotation angle in $NdAlO_3$; data from Ref. 10.

C. Comparisons with other $R\bar{3}c$ perovskites

The perovskite structure is adopted by a wide range of ternary compounds, usually in one of its distorted forms. Several authors have systematically reviewed the various perovskite hettotypes where the cubic symmetry is broken by octahedral tilting.[5,46,47] By far the most common hettotype has the space group *Pnma*, corresponding to a tilt system $a^-b^+a^-$. For *Pnma* perovskites, the tilt angles are accurately modeled by bond valence calculations.[46] Similar calculations do not describe $R\bar{3}c$ perovskites correctly. From this, Lufaso and Woodward[47] conclude that the $a^-b^+a^-$ perovskite tilt system is driven by the valence requirements of the *A*-site cation, but that some other factor causes the $a^-a^-a^-$ tilt system to occur. One possibility is that the transition is dominated by the distortion of the AlO_6 octahedra and that this drives the octahedral rotation as a secondary process. This difference could be the origin of the rather large energy scale of the phase transition in $LaAlO_3$, noted above.

A phase transition from the $R\bar{3}c$ structure to the cubic perovskite aristotype has been studied in a number of other oxide perovskites.[7,16,48] Temperature-dependent structural

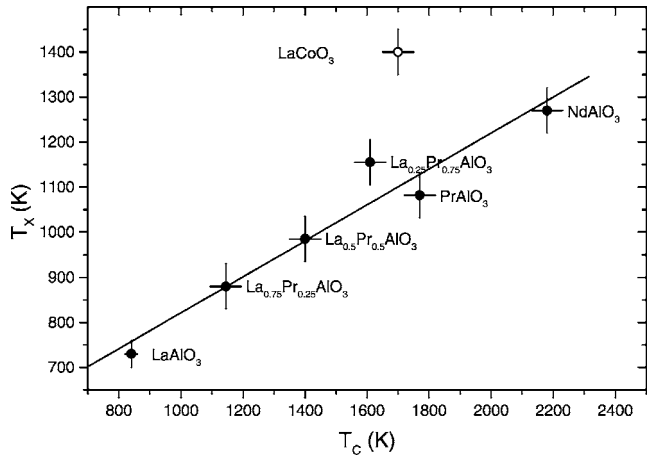

FIG. 28. Correlation between the temperature of anomaly in $\phi(T)$, T_X, and the $Pm\bar{3}m$-$R\bar{3}c$ transition temperature T_C, for a range of perovskites.

data exist for several materials, including $NdAlO_3$ and $PrAlO_3$,[10] the $La_xPr_{1-x}AlO_3$ solid solution,[49] $LaGaO_3$,[50] and $LaCoO_3$.[51,52] In all these systems, the theoretical relationship $\phi^2 \propto e_4 \propto (1-\eta)$ fails, and the underlying reason for this is the form of $\phi^2(T)$. The published data for each system are generally rather sparse. One interpretation of these data is that the $\phi^2(T)$ graph has two linear sections, as in $LaAlO_3$. This is shown for $NdAlO_3$ in Fig. 27.

In each material, we may identify (at least approximately), a crossover temperature T_X in the $\phi^2(T)$ graph; in $NdAlO_3$, this is approximately 1270 K. Making the hypothesis that the underlying mechanism for this anomaly is the same in all these materials, we plot T_X against T_C for various $R\bar{3}c$ perovskites in Fig. 28. There is an approximately linear correlation between T_C and T_X for most of the samples. $LaAlO_3$ is a rather stable perovskite structure; of the $A^{3+}B^{3+}O_3$ perovskites surveyed by Cheng and Navrotsky,[53] it has the largest enthalpy of formation, most nearly perfect packing of La[12] and Al[6], and remains cubic to the lowest temperature of this family of perovskites. Other compositions lead to perovskites which are inherently more distorted (so that the cubic-rhombohedral transition temperature is higher), which apparently also favors the preservation of vacancy clustering to higher temperatures, though more investigations of this effect are clearly necessary.

[1] E. K. H. Salje, *Phase Transitions in Ferroelastic and Co-elastic Crystals* (Cambridge University Press, Cambridge, UK, 1990).
[2] M. A. Carpenter, Rev. Mineral. Geochem. **39**, 35 (2000).
[3] S. A. T. Redfern, Rev. Mineral. Geochem. **39**, 105 (2000).
[4] M. A. Carpenter, E. K. H. Salje, and A. Graeme-Barber, Eur. J. Mineral. **4**, 621 (1998).
[5] A. M. Glazer, Acta Crystallogr., Sect. B: Struct. Crystallogr. Cryst. Chem. **28**, 3384 (1972).
[6] C. N. W. Darlington, Phys. Status Solidi A **155**, 31 (1996).
[7] S. Geller and V. B. Bala, Acta Crystallogr. **9**, 1019 (1956).
[8] E. A. Wood (private communication cited in Ref. 7); see also Am. Mineral. **36**, 768 (1951).
[9] K. A. Müller, W. Berlinger, and F. Waldner, Phys. Rev. Lett. **21**, 814 (1968).
[10] C. J. Howard, B. J. Kennedy, and B. C. Chakoumakos, J. Phys.: Condens. Matter **12**, 349 (2000).
[11] B. C. Chakoumakos, D. G. Schlom, M. Urbanik, and J. Luiane, J. Appl. Phys. **83**, 1979 (1998).
[12] H. Lehnert, H. Boysen, J. Schneider, F. Frey, D. Hohlwein, P. Radelli, and H. Ehrenberg, Z. Kristallogr. **215**, 536 (2000).
[13] S. Bueble, K. Knorr, E. Brecht, and W. W. Schmahl, Surf. Sci. **400**, 345 (1998).
[14] J. Chrosch and E. K. H. Salje, J. Appl. Phys. **85**, 722 (1999).
[15] S. A. Hayward, S. A. T. Redfern, and E. K. H. Salje, J. Phys.: Condens. Matter **14**, 10131 (2002).
[16] J. F. Scott, Phys. Rev. **183**, 823 (1969).
[17] P. Bouvier and J. Kreisel, J. Phys.: Condens. Matter **14**, 3981 (2002).
[18] J. Zhao, N. L. Ross, and R. J. Angel, J. Phys.: Condens. Matter **16**, 8763 (2004).
[19] E. K. H. Salje, B. Wruck, and H. Thomas, Z. Phys. B: Condens. Matter **82**, 399 (1991).
[20] J. M. Pérez-Mato and E. K. H. Salje, Philos. Mag. Lett. **81**, 885 (2001).
[21] E. Salje and V. Devarajan, Phase Transitions **6**, 235 (1986).
[22] D. C. Palmer, U. Bismayer, and E. K. H. Salje, Phys. Chem. Miner. **17**, 259 (1990).
[23] S. A. Hayward and E. K. H. Salje, Phase Transitions **68**, 501 (1999).
[24] M. Geday, J. Kreisel, A. M. Glazer, and K. Roleder, J. Appl. Crystallogr. **33**, 909 (2000).
[25] H. W. Meyer, M. A. Carpenter, A. Graeme-Barber, P. Sondergeld, and W. Schranz, Eur. J. Mineral. **12**, 1139 (2000).
[26] Y.-C. Chang, D.-S. Hou, Y.-D. Yu, S.-S. Xie, and T. Zhou, J. Cryst. Growth **129**, 362 (1993).
[27] H. Newton (private communication).
[28] R. M. Ibberson, W. I. F. David, and K. S. Knight, The High Resolution Neutron Powder Diffractometer (HRPD) at ISIS—A User Guide Report No. RAL-92-031, 1992 (unpublished).
[29] A. C. Larson and R. B. Von Dreele, Los Alamos National Laboratory Report No. LAUR 86-748, 2000 (unpublished).
[30] R. R. Reeber, K. Goessel, and K. Wang, Eur. J. Mineral. **7**, 1039 (1995).
[31] M. A. Carpenter, A. I. Becerro, and F. Seifert, Am. Mineral. **86**, 348 (2001).
[32] H. D. Megaw and C. N. W. Darlington, Acta Crystallogr., Sect. A: Cryst. Phys., Diffr., Theor. Gen. Crystallogr. **31**, 161 (1975).
[33] S.-Y. Cho, I.-T. Kim, and K. S. Hong, J. Mater. Res. **14**, 114 (1999).
[34] J. T. S. Irvine, D. C. Sinclair, and A. R. West, Adv. Mater. (Weinheim, Ger.) **2**, 132 (1990).
[35] K. Nomura and S. Tanase, Solid State Ionics **98**, 229 (1997).
[36] A. Aird and E. K. H. Salje, J. Phys.: Condens. Matter **10**, L377 (1998).
[37] S. Zafar, R. E. Jones, B. Jiang, B. White, P. Chu, D. Taylor, and S. Gillespie, Appl. Phys. Lett. **73**, 175 (1998).
[38] R. J. Harrison, S. A. T. Redfern, and E. K. H. Salje, Phys. Rev. B **69**, 144101 (2004).
[39] A. M. Glazer, J. G. Lewis, and W. Kaminsky, Proc. R. Soc. London, Ser. A **452**, 2751 (1996).
[40] M. A. Geday and A. M. Glazer, J. Phys.: Condens. Matter **16**, 3303 (2004).
[41] M. V. Abrashev, A. P. Litvinchuk, M. N. Iliev, R. L. Meng, V. N. Popov, V. G. Ivanov, R. A. Chakalov, and C. Thomsen, Phys. Rev. B **59**, 4146 (1999).
[42] D. I. Woodward, I. M. Reaney, G. Y. Yang, E. C. Dickey, and C. A. Randall, Appl. Phys. Lett. **84**, 4650 (2004).
[43] C. A. McCammon, A. I. Becerro, F. Langenhorst, R. J. Angel, S. Marion, and F. Seifert, J. Phys.: Condens. Matter **12**, 2969 (2000).
[44] C. L. Jia and K. Urban, Science **303**, 2001 (2004).
[45] D. W. Deis, J. K. Hulm, and C. K. Jones, Bull. Am. Phys. Soc. **14**, 61 (1969).
[46] P. M. Woodward, Acta Crystallogr., Sect. B: Struct. Sci. **53**, 44

(1997).
[47] M. W. Lufaso and P. M. Woodward, Acta Crystallogr., Sect. B: Struct. Sci. **57**, 725 (2001).
[48] S. Geller and P. M. Raccah, Phys. Rev. B **2**, 1167 (1970).
[49] B. J. Kennedy, C. J. Howard, A. K. Prodjosantoso, and B. C. Chakoumakos, Appl. Phys. A **74**, S1660 (2002).
[50] C. J. Howard and B. J. Kennedy, J. Phys.: Condens. Matter **11**, 3229 (1999).
[51] G. Thornton, B. C. Tofield, and A. W. Hewat, J. Solid State Chem. **61**, 301 (1986).
[52] Y. Kobayashi, T. Mitsunaga, G. Fujinawa, T. Arii, M. Suetake, K. Asai, and J. Harada, J. Phys. Soc. Jpn. **69**, 3468 (2000).
[53] J. Cheng and A. Navrotsky, J. Mater. Res. **18**, 2501 (2003).